AGU ADVANCING EARTH AND SPACE SCIENCES

Water Resources Research

RESEARCH ARTICLE
10.1029/2024WR038657

Evolution of Erosion and Deposition Induced by an Impinging Jet to Manage Sediment

P. Buffon[1,2], W. S. J. Uijttewaal[1], D. Valero[3], and M. J. Franca[2]

[1]Faculty of Civil Engineering and Geosciences, Delft University of Technology, Delft, The Netherlands, [2]Institute for Water and Environment, Karlsruhe Institute of Technology, Karlsruhe, Germany, [3]Faculty of Engineering, Imperial College London, London, UK

Key Points:

- Direct and indirect transport modes for suspended sediment from the scour hole were identified and quantified
- Self-similarity of longitudinal bed profiles is demonstrated for the erosion and deposition areas during the indirect transport mode
- We propose a scalable measure for the net sediment volume displacement resulting from the jet application

Supporting Information:

Supporting Information may be found in the online version of this article.

Correspondence to:

P. Buffon and W. S. J. Uijttewaal,
p.buffon@tudelft.nl;
w.s.j.uijttewaal@tudelft.nl

Citation:

Buffon, P., Uijttewaal, W. S. J., Valero, D., & Franca, M. J. (2025). Evolution of erosion and deposition induced by an impinging jet to manage sediment. *Water Resources Research*, *61*, e2024WR038657. https://doi.org/10.1029/2024WR038657

Received 29 AUG 2024
Accepted 14 MAR 2025

Abstract Dams are important water infrastructure whose main purposes can be compromised by sedimentation. This causes loss of storage volume, affecting river sediment fluxes and morphology. However, sediment management strategies can be implemented to reduce these impacts. Our goal is to characterize and quantify key processes of an idealized and reduced physical model of water injection dredging, applicable as a sediment management technique. Three sets of experiments were conducted, varying the following parameters: (a) jet discharge; (b) jet angle; (c) bed angle. The spatio-temporal evolution of the main physical processes (scour hole formation, sediment suspension development, and downstream deposition) was analyzed using images of profiles acquired during the experiments. We identified two distinct transport modes depending on how the jet flow connects with the turbidity current, each associated with different stages of scour hole development. In our experiments, the bed-perpendicular component of the exit velocity (momentum) of the jet is the primary driver of the morphological evolution. We demonstrate self-similarity in the longitudinal profiles of the scour hole and downstream deposit. Finally, we discuss practical implications of this study, such as the net displacement of the material, scaling, and limitations. This research contributes to the development of innovative sediment management strategies for water reservoirs and other hydraulic structures.

Plain Language Summary When constructing dams in rivers to create water reservoirs, a substantial amount of sand and mud can accumulate in the reservoir instead of flowing freely downstream. This can cause economic and environmental impacts, compromising the sustainability of the dam reservoir. We explore a new method using a water jet to relocate the settled sand and mud to a more suitable location, for instance, downstream of the dam in the river. In a laboratory, we built a small-scale version of this technique and conducted experiments under various scenarios of water jet speed, and jet and bed angle. By analyzing videos of the experiments, we identified distinct phases of the processes initiated by this technique, and we observed the sand moving in two different ways from the area around the water jet to downstream. Our findings indicate that under the variables studied, the speed of the water jet plays a crucial role in determining how far the sand travels. This insight can contribute to improving the effectiveness of water jet applications in water reservoirs and similar environments. As a consequence, it has the potential to extend the life of a dam reservoir, contributing to water and energy availability.

1. Introduction

There are over 60,000 large dams in the world (ICOLD, 2024) for the purposes of: irrigation, energy production, water supply, flood control, among others. In addition, they are considered adaptation measures to the growing risks associated with the changes in the water cycle due to global warming and to the global increasing water demand (Boulange et al., 2021; Burke et al., 2023; Caretta et al., 2022; Wisser et al., 2013). Despite their multiple important functions, these hydraulic infrastructures require careful consideration due to (sometimes irreversible) negative environmental impacts (Baena-Escudero et al., 2021; Ezcurra et al., 2019; Latrubesse et al., 2017; Ma et al., 2022; Schmitt et al., 2018; Zarfl et al., 2019).

The interruption of the natural sediment flux is one of the major dam impacts when impounding the valley for the formation of a reservoir. Reservoirs are hence subjected to sedimentation (Fan & Morris, 1992; Schleiss et al., 2016; Syvitski et al., 2005; Wisser et al., 2013), which leads or contributes to: changes in downstream fluvial and coastal morphology (Warrick et al., 2019), delta subsidence (Kondolf et al., 2022), and also loss of

storage, loss of capacity to attenuate downstream floods, hydro-abrasion of infrastructure components, among others (Annandale et al., 2016; Kondolf et al., 2014).

Sediment management techniques can be implemented to minimize the impacts caused by reservoir sedimentation and to favor inter-generational sustainability of hydraulic structures and water resources. They are traditionally classified into four categories (Annandale et al., 2016): (a) reduce sediment yield from upstream, (b) route sediments, (c) remove or redistribute deposits, and (d) adaptive strategies. Recent initiatives call for management approaches with a focus on maintaining the rivers' sediment connectivity (Kondolf et al., 2022; Randle et al., 2021; Shelley et al., 2022).

This research is mostly framed in the context of the third category, corresponding to the removal and redistribution of sediment deposits in the reservoir. We focus on an emerging sediment management technique called water injection dredging, where a water jet impinges on the bed, mobilizes the sediment, and triggers a turbidity current (PIANC, 2013). This turbidity current can convey the mobilized sediments and eventually vent it through the dam outlet, a technique under the second category, route sediments, traditionally used to vent natural turbidity currents (Chamoun et al., 2018).

Other sediment management techniques applying hydrodynamic processes to mobilize sediment and evacuate it through the dam section are an economically and environmentally viable option for managing reservoir sedimentation (Kondolf et al., 2014; Shelley et al., 2022). More specifically, water injection dredging was reported to be successful in two reservoirs in China (Wang & Hu, 2009): in the Sanmenxia Reservoir, to locally redistribute sediment deposits; and in the Xiaolangdi Reservoir, to vent the triggered turbidity current. However, most applications of this technique, and from where most of the knowledge on the technique ensues, are carried out in estuarine environments such as Port of Rotterdam in the Netherlands (Kirichek et al., 2021), where pilot projects where recently carried out.

The generation of turbidity currents by water jets for sediment management purposes in water reservoirs was studied by Sequeiros et al. (2009). However, the (fixed) jets applied in that study were wall jets, differing from water injection, in which the jet is positioned at a fixed distance from the mobile bed and impinges at an angle. Water injection by a traveling jet into sediment for cable burial applications was studied by Perng and Capart (2008), although with the goal to suspend the sediment locally, not to transport it to distal areas by a turbidity current. To the best of our knowledge, a full description and quantification of the main processes related to the application of this technique does not exist. This lack of scientific knowledge hinders the application of such a technique with a potential to contribute to an efficient removal of sediment from reservoirs.

The technique of triggering turbidity currents by impinging water jets involves complex processes (Kirichek et al., 2021; Winterwerp et al., 2002). Our investigation is based on an idealized concept as illustrated in Figure 1a, where three major processes are identified: erosion of a scour hole induced by the momentum of the impinging water jet; transport in suspension of the eroded material to a turbidity current downstream, which transports the material via buoyancy-driven forces; and deposition due to an excess supply of sediment to the turbidity current. Some deposition can occur upstream of the scour hole as well. Hence, this study will focus on the impinging jet momentum conditions (angle and strength), and consequent distal sediment transport conditions which, in this case, will be affected by the inclination of the bed.

Scour erosion and deposition by turbidity currents have been extensively discussed in the literature as independent fields of study. Based on the work of, for instance, Di Nardi et al. (2022); Pagliara et al. (2008); Rajaratnam and Mazurek (2002) we identify key geometrical components of the scour hole evolution as in Figure 1b. For the turbidity current region, we will investigate the longitudinal shape of the deposit. This shape was inferred to be exponential by Nomura et al. (2022); Pirmez and Imran (2003); Rooij et al. (2009), whereas Birman et al. (2009) concluded that it can also have a power law shape depending on water entrainment considerations. The mass balance is eventually governed by erosion and deposition, so it is interesting to assess the efficiency of the injection dredging technique without the need to include details of the turbidity current itself.

In this investigation, we use a schematized and reduced-scale physical modeling approach in order to quantify the scouring and deposition processes, and the relationship between them. We aim to address this knowledge gap by investigating how the erosion of the scour hole and the downstream deposition relates to the jet characteristics and bed angle. We reach this goal by answering the following questions:

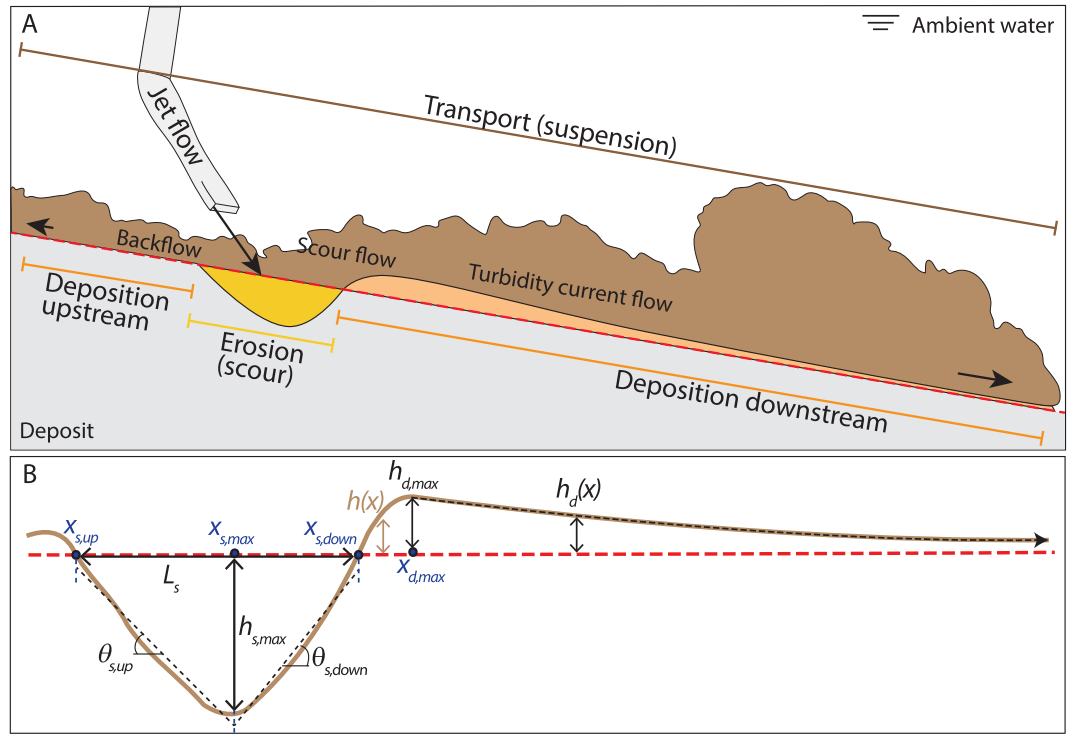

Figure 1. (a) Sketch of the physical system under analysis with definition of the three major processes: erosion of a scour hole, transport of the eroded sediment in suspension (scour and turbidity current flows), and downstream deposition. (b) Sketch defining the main variables concerning the immediate morphodynamic changes (scour hole erosion and downstream deposition). Nomenclature: $h(x)$ is the longitudinal profile; L_s is the scour hole length at the initial bed elevation (dashed red line); $h_{s,max}$ is the scour hole depth; $\theta_{s,up}$ is the angle of the upstream face of the scour hole; $\theta_{s,down}$ is the angle of the downstream face of the scour hole; $h_{d,max}$ is the thickness of the highest point of the deposit, called ridge or dune; $h_d(x)$ is the downstream deposit shape function in the turbidity current region; x is the horizontal position of the upstream $(x_{s,up})$ and downstream $(x_{s,down})$ intersections of the longitudinal bed profile with the initial bed level profile (dashed red line), and of the deepest $(x_{s,max})$ and highest $(x_{d,max})$ points of the profile.

1. What is the spatio-temporal evolution of the erosion and deposition processes?
2. How is the spatio-temporal evolution of these processes affected by changing initial (i.e., bed angle) and boundary conditions (i.e., jet momentum and angle)?
3. What is the material displacement resulting from the jet application?

Although the in-depth study of the sediment suspension transport is out of the scope of this article, we intend to also provide a general description of the transport mode at the scour flow region (see Figure 1a).

2. Materials and Methods

2.1. Experimental Setup

In our experiments, we opted for an idealized configuration with reduced complexity, similarly to Perng and Capart (2008). This configuration aimed at simulating the spatio-temporal evolution of key features of the scouring and depositional processes (as illustrated in Figure 1) in a controlled and monitored setting. We used a 2D-vertical configuration, static jet, and homogeneous deposit composed of uniform non-cohesive sediment excluding any biological processes. As a consequence, the research questions pertain to the variation of a limited set of parameters, which limits the scope of the research. We considered the Shields number criteria for sediment erosion, the Rouse number criteria for sediment suspension, and the Reynolds number criteria for self-similar jet flow (Hughes, 1995; Julien, 2002). Implications of these design choices will be discussed in the results and discussion section.

The experimental investigation was performed in a 4 m long, 0.22 m wide (W) and 2 m deep flume (Figure 2a), installed in the Hydraulic Engineering laboratory of Delft University of Technology. The downstream section of

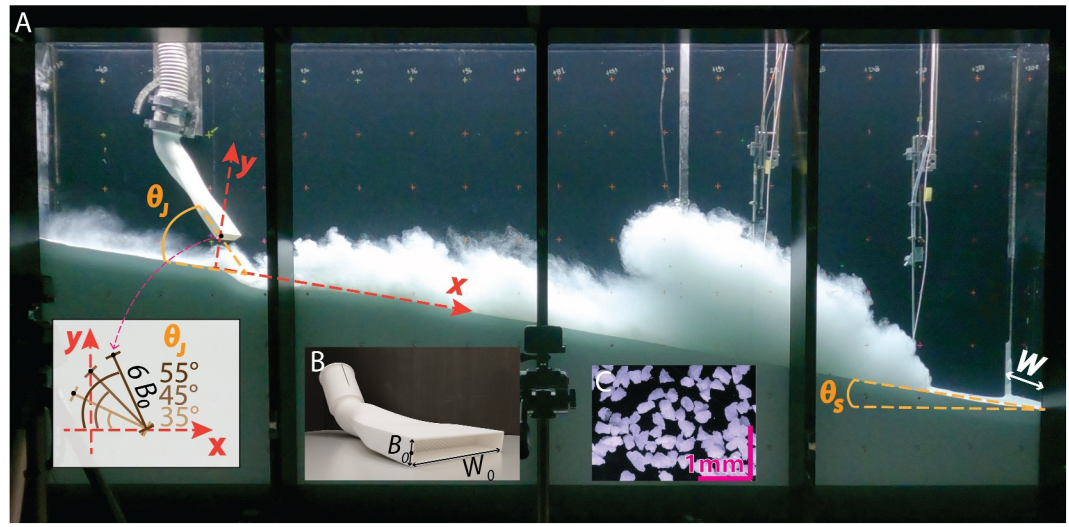

Figure 2. (a) Experimental flume of width (W) 0.22 m, height 2 m and length 4 m, showcasing a running experiment ($Q3J45S10$, see Table 1) with indication of the coordinate system and the geometrical variables of this study, impingement angle of the jet θ_J, and angle of the mobile bed θ_S; a sketch illustrates the relative position of the jet when changing its angle. Inset (b) 3D printed jet mouth piece with jet width $W_0 = 0.2$ m and thickness $B_0 = 0.03$ m. Inset (c) microscopic image of the light-weight sediment.

the flume is connected to a reception tank (2.50 m deep, 1.25 m wide and 1.25 m long) where the out-flowing turbidity current is absorbed. This tank is equipped with an overflow weir to ensure a constant water level during the experiment, at 1.95 m from the bottom of the flume.

A 3D printed diffuser (Figure 2b) with a rectangular outlet with dimensions 0.2 m wide (W_0) and 0.03 m thick (B_0) reproduces a 2D planar jet across the flume. The upstream end has a circular cross-section with 90 mm of internal diameter and 45° bend. Via a flexible pipe with same internal diameter, the flow is fed directly from the laboratory pipeline system connected to a constant level water reservoir, which guarantees constant inflow for the duration of the experiment. More details on the diffuser design and its validation as a 2D planar jet can be found on the Figure S1 and Text S1, respectively, in Supporting Information S1. Therefore, this design with a rectangular nozzle allows a direct inference of the main flow characteristics.

Other alternatives, such as a multi-port diffuser with an array of circular nozzles (Perng & Capart, 2008), were less attractive because, although flows from an array of circular nozzles are expected to merge and form a plane jet, the design features of this type of diffuser add three dimensional aspects to the flow (Jirka, 2006), and the establishment of basic boundary conditions is more complex. In addition, according to Perng and Capart (2008), the multi-port configuration could lead to asymmetric erosion in the transversal direction if not precisely adjusted. Our design, on the other hand, presented a robust and compact device alternative, which could safely be transported in, out, and along the flume—as required during the experimental campaign.

The 2D-plane Cartesian coordinate system—x for the streamwise direction, aligned with the initial bed with angle θ_S, and y for the direction perpendicular to the bed—is shown in Figure 2a. The coordinate of the impingement intersection with the initial bed is ($x = 12.7$ cm, $y = 0$ cm) for all experiments. The center line of the jet flow intersects the initial bed 18 cm from the jet orifice for all experiments. This distance corresponds approximately to the end of the potential core, $\approx 6B_0$ (Rajaratnam, 1976), so the erosion is caused by a fully developed jet flow. For the case with jet angle = 45°, the coordinate of the center of the jet exit ($B_0/2$) is ($x = 0$ cm, $y = 12.7$ cm). When the jet angle (θ_J) is set differently (35° and 55° in the present investigation), the coordinates of the center of the jet exit are adjusted accordingly (see sketch in Figure 2a).

2.2. Sediment and Deposit Characteristics

The mobile bed is composed of non-cohesive light-weight particles (Figure 2c), decreasing the required jet momentum input in the flume to enable sediment erosion and transport. The dry density of this material (ρ_{sed}) is

Table 1
Experimental Settings Varying Q_0, θ_J, and θ_S

Experiment	Q_0 (l/s) ± 0.02 l/s	θ_J (°) ± 1°	θ_S (°) ± 0.5°	U_0 (m/s)	M_0 (N/m)	$Re_0(10^3)$	$Fr_{d,0}$
Q1J45S00	0.99	45	0.0	0.16	0.8	4.9	4.6
Q2J45S00	1.95	45	0.0	0.32	3.1	9.7	9.1
Q3J45S00	**2.97**	**45**	**0.0**	**0.49**	**7.3**	**14.8**	**13.9**
Q4J45S00	4.02	45	0.0	0.67	13.4	20.1	18.8
Q5J45S00	5.08	45	0.0	0.85	21.5	25.4	23.7
Q3J35S00	2.95	35	0.0	0.49	7.2	14.7	13.8
Q3J55S00	2.94	55	0.0	0.49	7.2	14.7	13.8
Q3J45S03	2.96	45	3.3	0.49	7.3	14.8	13.9
Q3J45S10	2.96	45	10.1	0.49	7.3	14.8	13.8
Q3J45S17	2.95	45	16.7	0.49	7.3	14.8	13.8

Note. Jet exit velocity, $U_0 = \frac{Q_0}{B_0 W_0}$; momentum flux per unit width, $M_0 = \rho U_0^2 B_0$; Reynolds number, $Re_0 = \frac{U_0 B_0}{\nu}$; and densimetric Froude number, $Fr_{d,0} = \frac{U_0}{\sqrt{g' D_{50}}}$; where B_0 and W_0 are the jet's exit thickness (0.03 m) and width (0.2 m), respectively, ν is the kinematic viscosity of water (10^{-6} m^2/s), ρ is the density of the water (998 kg/m^3), D_{50} is the characteristic grain size (0.222 10^{-3} m), and $g' = g\frac{\rho_{sed} - \rho}{\rho}$ is the reduced gravitational acceleration; with $g = 9.81$ m/s^2, and the dry density of sediment $\rho_{sed} = 1581$ kg/m^3.

1,581 kg/m^3 (±0.5%). The particles' size range between 150 and 300 μm with characteristic diameters of $D_{10} = 185$ µm ± 0.5%, $D_{50} = 222$ µm ± 1% and $D_{90} = 271$ µm ± 3%, and settling velocities (ω) ranging between 0.5 and 1.9 cm/s ± 8%. The submerged angle of repose of the sediment (θ_{cr}) is 33° ±5%.

The initial bed is built flat under water with the use of a laser level and a flat wiper. It is constructed with an imposed inclination, and is smoothened such that it is uniform across the flume width. It has a separately measured dry bulk density, that is, the mass of water in the pores is not accounted for, $(\rho_{d,0})$ of 735 kg/m^3 ± 2%. This initial high dry bulk density of the bed is achieved by compaction with a commercial concrete vibrator. The new deposit, generated by the settling of the suspended sediment, has a separately measured dry bulk density of $(\rho_{d,new})$ 564 kg/m^3 (±1%). The respective wet bulk densities, which account for the mass of water in the pores, are 1,269 and 1,206 kg/m^3.

More details about how these sediment and deposit characteristics were determined can be found on the Texts S2 and S3, respectively, in Supporting Information S1.

2.3. Experiments

Ten different experiments were performed. A base case is selected for reference to assist in the comparison in the results section which has characteristics: $Q_0 = 3$ l/s, $\theta_J = 45°$, $\theta_S = 0°$. This experiment is highlighted in Table 1. Three groups of experiments can thus be identified, varying with respect to the base case (Table 1):

1. Varying the discharge of the jet (Q_0) from 1 to 5 l/s;
2. Varying the impingement angle of the jet (θ_J) from 35 to 55°;
3. Varying the initial angle of the bed (θ_S) from 0 to 17°.

We set $\theta_J = 45°$ for the base case hypothesizing that this would be an optimum distribution of momentum to favor both scour erosion and downstream transport. We further test this hypothesis by varying θ_J below and above the base case value. Apart from this, the highest discharge and slope values relate to the flume capacity, while keeping important experimental design features the same for all experiments.

The procedure near the start of the experiment consisted of (a) installing the jet in the flume, with its vertical position well above the bed (≈ 50 cm); (b) suctioning water from the flume through the jet and its flexible pipe in order to fill them with water and remove air, (c) lowering the jet to the correct initial position of the experiment; (d) setting the discharge to the desired value through a calibrated parallel pipe; (e) turning on the data acquisition

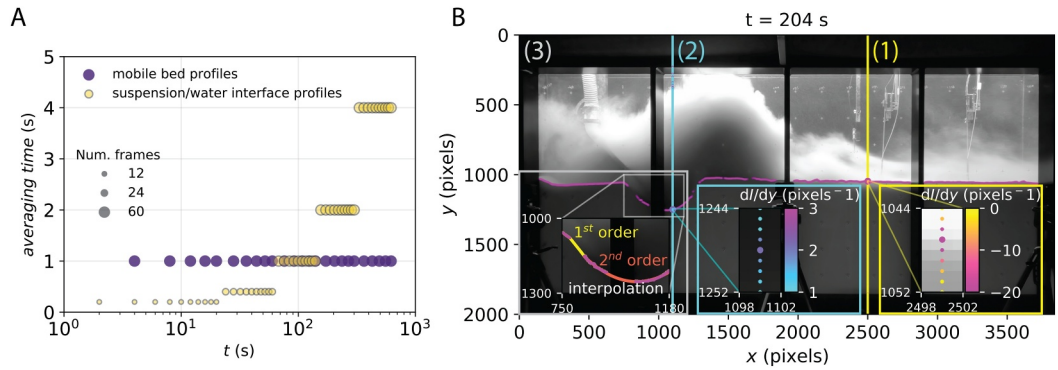

Figure 3. (a) Data acquisition moments from the videos. The *t* axis shows the sampling frequency on a logarithmic scale, the size of circles indicate the number of frames extracted, and *averaging time* indicates the size of the time window from which the frames were extracted and averaged. (b) Example from experiment *Q3J45S00* of a bed level profile extraction from a 1 s (60 frames) averaged image. The two vertical colored lines are examples of the spatial pixel intensity (*I*) gradient (calculated from top to bottom), and the zoom in boxes show details of: identification of the (a) minimum and (b) maximum gradient; and (c) first and second order interpolations applied where data were missing.

equipment; (f) opening the valve to let the water flow through the jet, starting the experiment. After a few minutes (9–11 min) this valve was closed, finishing the experiment.

2.4. Data Acquisition

The inflow discharge is measured by a flow meter (Endress + Hauser Prosonic Flow 91W "Clamps-on" version, accuracy ±2%, sampling frequency = 100 Hz) installed in the upstream pipes connecting the hydraulic circuit from the laboratory to the jet. Data is acquired through a logger (MC Measurement Computing USB-1608G) and the acquisition software (Data Acquisition System Laboratory—DASYLab), except for the video recordings.

The measurements that are the basis for the present analysis are the temporal evolution of the bed level topography and the interface between the sediment suspension and the ambient water. These profiles were obtained through images acquired with a digital camera (GoPro HERO 9) with the same field of view of Figure 2a. The camera was set to 59.94 fps and 4K resolution (3,840 × 2,160 pixels). The videos and discharge time series are synchronized via an LED-generated light pulse.

2.5. Extraction of Longitudinal Profiles

Figure 3a shows the profiles' extraction frequency from the video recordings by plotting the sampling time moments (*t*) along the time series. This frequency is higher for the suspension/water interface profiles case to account for the higher unsteadiness of the process; and for both mobile bed and suspension/water interface profiles cases, this frequency reduces over time, as the scour hole increases with the logarithm of time eventually toward an asymptotic state (Rajaratnam & Berry, 1977). In addition, Figure 3a shows the number of frames utilized for the extraction of each profile (indicating the sufficient number of samples to average), and the size of the time window (*averaging time*) from which they were extracted and averaged (accounting again for the unsteadiness of the processes).

To extract the bed level profiles, a semi-automated script was developed in Python programming language (version 3.8). The light intensity of the red channel from a time averaged image in RGB color mode (i.e., Red, Green, and Blue) was used (e.g., Figure 3b) since this was found to provide the clearest contrast between the bed and the outer flow. The bed level was identified from the interface where the largest change in intensity between consecutive pixels could be found. This was executed by computing from top to bottom the vertical spatial gradient of the pixel intensity, and identifying as the bed level the negative peak around the transition between the suspension and the deposit (e.g., Figure 3b1). In some regions, the positive peak was identified (e.g., Figure 3b2) if the suspension above the deposit was concentrated enough to reduce its light intensity to lower levels than the deposit. Spurious data points were identified visually and manually selected using a mouse lasso selector tool (Matplotlib library, version 3.3.4), and then excluded. As the suspended material is subject to turbulent motions

and entrainment of ambient water, the standard deviation (instead of the average) of the intensity variations in subsequent images was used to determine the position of the upper interface.

The resolution of this technique to extract the longitudinal profiles is comparable to the pixel size (≈1 mm), but other factors play a more important role in the uncertainty of this technique. For instance, the uniformity of the deposit level across the width of the flume and the amount of spurious data points (which increases with the sediment concentration in suspension) play an important role in the accuracy of the bed level profiles. These uncertainties are difficult to accurately quantify, but the uncertainty quantification of the subsequent analyses and interpretations encompasses them, not limiting the overall accuracy of the findings.

For calibration purposes, reference marks (crosses) were drawn on the glass window of the flume with a 20 cm grid. The pixel coordinate of the center of each cross was obtained via a capturing mouse clicks tool (OpenCV library, version 4.0.1). The process was repeated three times, and the average value was used in a linear interpolation to convert the pixel coordinates into the chosen coordinate system shown in Figure 2a.

Finally, where data were missing on the bed level profiles, a second order interpolation was implemented at the region around the maximum depth of the scour hole in case a structural pillar was in front of the glass (e.g., Figure 3b3). This assists in order to determine the location of the maximum depth of the scour hole. However, a first order interpolation was applied everywhere else. For the suspension interface profiles, where data was missing, a first order interpolation was applied, then a moving average with window size of 150 pixels (≈15 cm) was applied to smoothen the profile and improve the visualization.

2.6. Mass Balance

The mass of sediment that is eroded from the scour hole (m_s) is transported and eventually deposits downstream ($m_{d,down}$)—just next to the downstream edge of the scour hole ($m_{d,dun}$) or further downstream ($m_{d,exp}$)—and a small fraction upstream of the scour hole ($m_{d,up}$). The fraction of the eroded material found in suspension (m_{susp}) is also expected to be small. The conservation of sediment mass is expressed as the sum of these contributions by Equation 1:

$$m_s(t) = m_{d,dun}(t) + m_{d,exp}(t) + m_{d,up}(t) + m_{susp}(t). \tag{1}$$

While the total eroded and deposited sediment masses increase with time, the sediment mass in suspension is approximately constant. Hence, after a short period of time, the amount of sediment that is in suspension (m_{susp}) is considered small compared to the other terms in the equation and is therefore neglected. With reference to Equation 1, the contributions can be calculated from the geometric changes of the bed profile with respect to the initial conditions. The obtained areas can be related to the masses by taking into account the width W of the flume and the dry mass densities of the eroded $\rho_{d,0}$ and deposited $\rho_{d,new}$ material. Each contribution is then defined through:

$$\frac{m_s(t)}{W} = \rho_{d,0} \int_{x_{s,up}}^{x_{s,down}} (h(x, t=0) - h(x,t))\mathrm{d}x, \tag{2}$$

$$\frac{m_{d,up}(t)}{W} = \rho_{d,new} \int_{wall}^{x_{s,up}} (h(x,t) - h(x, t=0))\mathrm{d}x, \tag{3}$$

$$\frac{m_{d,dun}(t)}{W} = \rho_{d,new} \int_{x_{s,down}}^{x_{d,max}} (h(x,t) - h(x, t=0))\mathrm{d}x, \tag{4}$$

$$\frac{m_{d,exp}(t)}{W} = \rho_{d,new} \int_{x_{d,max}}^{\infty} h_{d,exp}(x,t)\mathrm{d}x. \tag{5}$$

The assumed exponential shape of the accumulated deposited material ($h_{d,exp}$) is given by Equation 6:

$$h_{d,exp}(x,t) = h_0(t) e^{-\frac{x - x_{d,max}}{L_{exp}}} \quad \text{for} \quad x > x_{d,max}, \tag{6}$$

where L_{exp} is the characteristic length scale. Equation 6 was fitted for each $h(x,t) - h(x,t=0)$ time series and for the spatial range $x > x_{d,max}$, and $h_0(t)$ is $h(x = x_{d,max},t) - h(x = x_{d,max},t = 0)$.

2.7. Sediment Mass Displacement

The net sediment mass displacement (L_{net}) in the x-direction of the chosen coordinate system was calculated as:

$$L_{net}(t) = x_{cm,down}(t) - x_{cm,s}(t) \tag{7}$$

where $x_{cm,down}$ is the position of the center of mass of the deposit downstream the scour hole, and $x_{cm,s}$ is the position of the center of mass of the scour hole. $x_{cm,down}$ was calculated as follows:

$$x_{cm,down}(t) = \frac{x_{cm,dun}(t)m_{d,dun}(t) + x_{cm,exp}(t)m_{d,exp}(t)}{m_{d,down}(t)} \tag{8}$$

where $x_{cm,dun}$ is the position of the center of mass of the deposit just next to the downstream edge of the scour hole, and $x_{cm,exp}$ is the position of the center of mass of the deposit further downstream. For completeness, this small portion of the downstream deposit located upstream the exponential fit starting point (see Figure 1b) is also included in the calculation of L_{net}, as it can have a larger influence during the early stages of the injection application. Both $x_{cm,s}$ and $x_{cm,dun}$ were calculated via numerical integration of vertical slices, while $x_{cm,exp} = x_{d,max} + L_{exp}$, where $x_{d,max}$ was extracted from the longitudinal profiles, and L_{exp} was obtained analytically through the fit of Equation 6.

Furthermore, when presented, the relative error or the variability of average values extracted from the data sets is determined using one standard deviation (i.e., relative error = standard deviation/average). These average values could be obtained for an ensemble or for a certain time interval. Additionally, when presented, the error bars represent the root mean square of the difference between the fitted line and the corresponding data points used for the fit calculation.

3. Results and Discussion

3.1. Erosion and Transport Patterns

In a first qualitative observation of the video recordings, different phases can be discerned that are connected to two modes of transport. The first phase is an initial unsteady phase (Figure 4a) characterized by the development and downstream advection of the head of the turbidity current, immediately followed by an unsteady/quasi-steady transition (Figure 4b) in which a continuous turbidity current is established (i.e., the head of the turbidity current is far away), but still subject to variations due to the development of the scour hole. This phase is interpreted as a transition to a more stable state, here called the quasi-steady phase (Figure 4c), which predominates over a longer period. During this period, the momentum of the jet is deflected by the shape of the scour hole and pushes the sediment upwards into a cloud, where the sediment load contributes to the stored potential energy, which feeds the turbidity current body (transport mode 2). This indirect transport mode is different from the modes observed in the preceeding stages, where a direct predominantly bed-horizontal transport of mass and momentum from the jet flow to the turbidity current is observed (transport mode 1).

We infer that shallower scour holes lead to a direct transport mode (pseudo-horizontal), while deeper scour holes lead to an indirect transport mode with an upstream sensibly vertical flux and intermediate storage in suspension (Figure 4). This can be explained by the increase of the angle of the downstream face of the scour hole to and beyond the angle of repose as the scour gets deeper, changing the direction of the outflow toward predominantly vertical, and increasing the height of the suspension cloud above the downstream edge of the scour hole. A similar upward flow pattern is visible as a major roller and bed roller, respectively, in the study of Mao et al. (2023).

Although the classification presented in Figure 4 was derived from visual observations of the suspension evolution at the scour flow region (see Figure 1a), the bed level at the same region (i.e., the scour hole) follows a

10.1029/2024WR038657

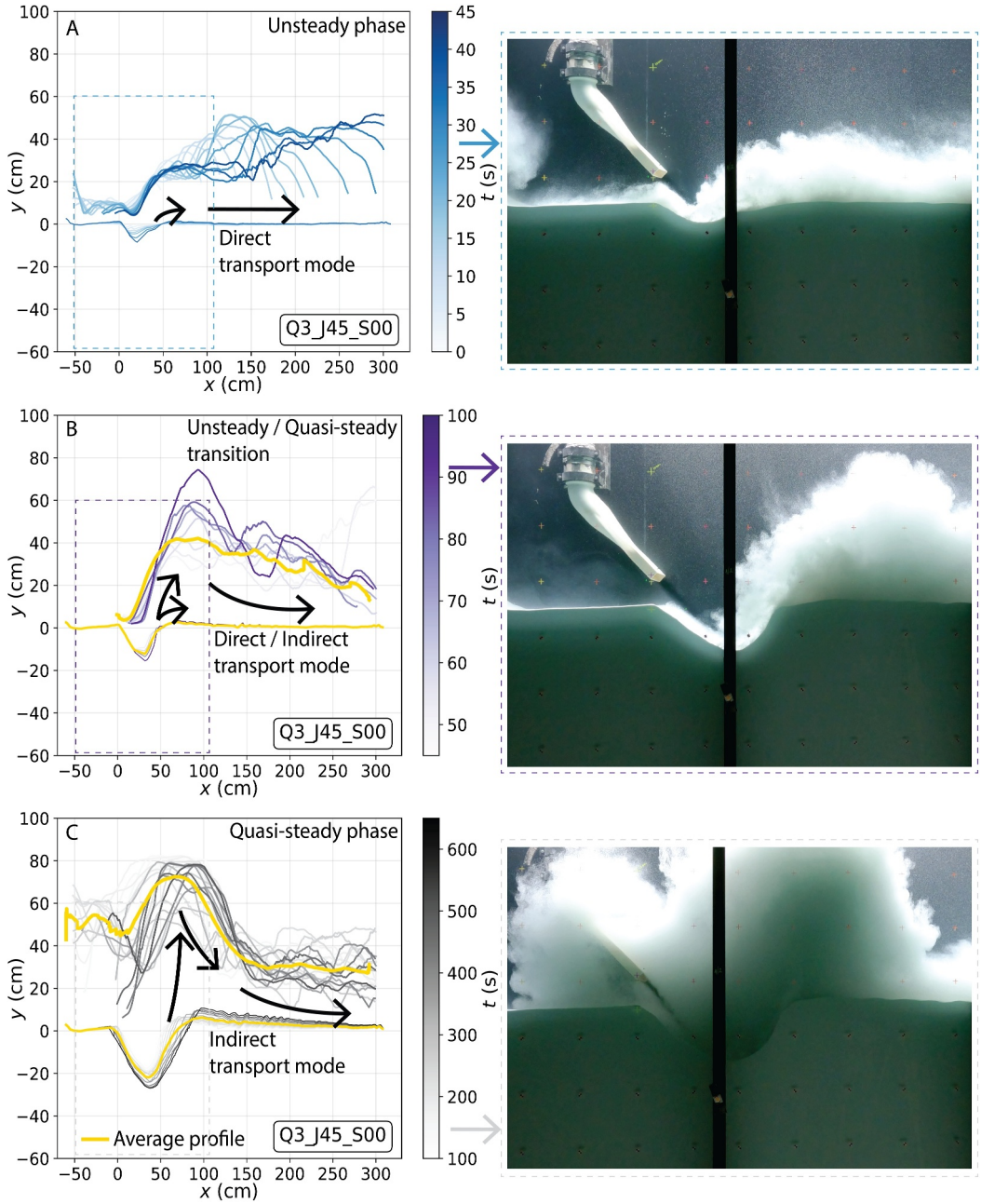

Figure 4. Illustration of bed level profiles, suspension/ambient water interface profiles, and the interpretation of flow patterns (black arrows) and different phases observed for the base case, *Q3J45S00*. (a, b) direct transport of momentum from jet to the turbidity current (transport mode 1), with: (a) Unsteady phase (phase 1)—turbidity current development (head passage), and (b) Unsteady/Quasi-steady transition phase—established turbidity current; (c) Quasi-steady phase (phase 2)—indirect transport of momentum from jet to turbidity current with upward movement and consequent collapse or plunging of the suspension into a turbidity current (transport mode 2). For each phase (a–c), a representative snapshot of the experiment is shown, corresponding to the dashed area on the left panels.

similar evolution pattern. Distinct patterns in the scour hole evolution have been reported in the literature by, for instance, (Bombardelli et al., 2018; Pagliara et al., 2008), who divided the scour hole evolution in two different stages before reaching equilibrium, which they termed: (a) developing, (b) developed. The main difference between these two stages is that the scour profiles are geometrically self-similar during the developed stage (Bombardelli et al., 2018; Di Nardi et al., 2022; Pagliara et al., 2008). These developing and developed stages

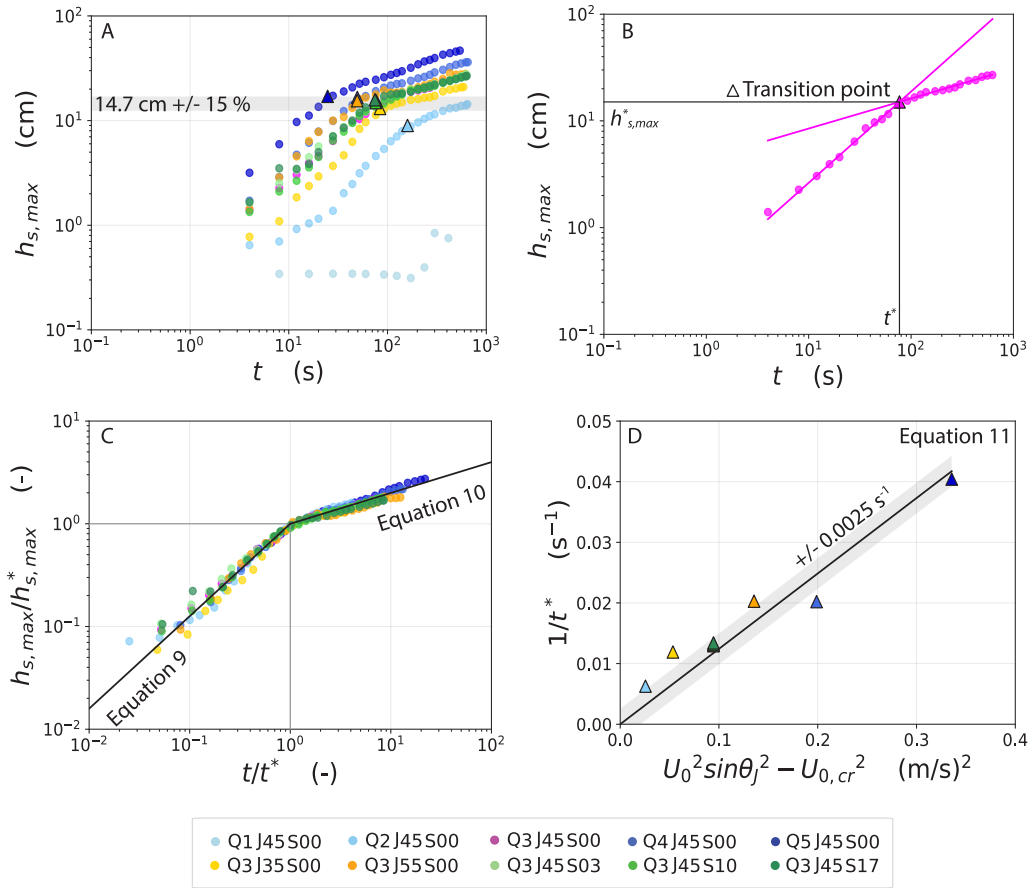

Figure 5. Temporal evolution of the scour hole. (a) Maximum depth of scour hole ($h_{s,\max}$) and transition points (triangles) with gray horizontal bar as the mean; (b) example of transition point ($h^*_{s,\max}$, t^*) determination for a single experiment (base case *Q3J45S00*); (c) dimensionless plot of $h_{s,\max}$ scale with transition point properties; (d) relationship between t^* and exit velocity (U_0).

appear to be linked to the direct (observed during the first phases) and indirect (observed during last phase) transport modes.

3.2. Scour Evolution

The main features defining the geometry of the scour hole are schematized in Figure 1b. We start by analyzing the maximum depth of the scour hole ($h_{s,max}$). Throughout the experiment's duration (<600 s), $h_{s,max}$ increases monotonically without reaching an asymptotic state. When analyzing the log-log time series of $h_{s,max}$ (Figure 5a), a slope break can clearly be identified as the transition between the initially rapid development followed by a slower but continuous growth, in line with the earlier identified transport modes 1 and 2 (Figures 4a and 4c).

For each experiment, the transition point (t^*, $h^*_{s,max}$) was determined at the intersection between two linear fits with different slopes, as exemplified in Figure 5b for the base experiment *Q3J45S00*. The points corresponding to values of $h_{s,max}$ below ≈2.72 cm were excluded from the fitting procedure to better capture the linear behavior near the transition point. Figure 5a shows that for most cases the transition occurs around a scour depth of $h^*_{s,max}$ = 14.7 cm ± 15%, indicating the change in behavior is strongly linked to the geometry of the hole. The clearly visible lower value of $h^*_{s,max}$ is the one with a relative low discharge *Q2J45S00*, while the experiment without a transition point is the experiment with the lowest discharge *Q1J45S00* and negligible transport.

The initial phase of erosion has a typical slope of approximately 0.9 (±10%), indicating an almost linear growth of the scour hole with time. Beyond the transition point, the slope reduces to an average value of 0.3 (±13%). These observations hold for all experimental settings as shown in Figure 5c. In summary:

$$\tilde{h}_{s,\max} = \frac{h_{s,\max}}{h^*_{s,\max}} \approx \left(\frac{t}{t*}\right)^{0.9} \quad \text{for} \quad t < t^*, \tag{9}$$

and

$$\tilde{h}_{s,\max} = \frac{h_{s,\max}}{h^*_{s,\max}} \approx \left(\frac{t}{t*}\right)^{0.3} \quad \text{for} \quad t > t^*, \tag{10}$$

where the tilde (˜) indicates a dimensionless property.

For the conditions of the present experiments, the transition time is inversely proportional to the bed-perpendicular component of the exit velocity of the jet squared, as shown in Figure 5d and Equation 11, where the constant C_u is ≈ 0.12 s/m^2. This relationship shows that the transition time tends to infinity when $U_0 \sin\theta_J$ tends to a minimum critical value $(U_{0,cr})$, under which no relevant erosion and deposition processes occur. Here, we adopted the value 0.16 m/s, the exit jet velocity from experiment $Q1J45S00$, as the minimum critical since the scour and turbidity current were found to be negligible in this case.

$$\frac{1}{t*} = C_u\left({U_0}^2 \sin{\theta_J}^2 - {U_{0,cr}}^2\right) \tag{11}$$

Similar to our experiments, Pagliara et al. (2008) identified a slope break when analyzing the evolution of the scour depth $h_{s,\max}/D_0$ as a function of $\log(t/T_R)$, where D_0 is the diameter of a round jet with $T_R = D_0/\sqrt{g' D_{90}}$ as the characteristic time. This slope break represented a transition time between the developing and developed states. They found the relationship $t^*/T_R = -0.78\theta_J^2 + 51.68\theta_J - 150$ as an estimate for the measured transition time. This implies a dependency on geometrical and material properties only.

The experimental conditions of Pagliara et al. (2008) were different from ours (mainly regarding: properties of the sediment, shape of the jet, 3D configurations, tailwater depth, and $Fr_{d,0}$ numbers). Applying their estimate to our experiments results in an overestimation of the transition time by a factor between 3 and 18. A major cause for this difference is found in the dominant role of the jet discharge in the current experiments whereas its influence on the transition time in the work of Pagliara et al. (2008) was considered negligible.

The identification of the two erosion modes proves effective within the specific time frame of our experiment. However, for $t/t^* > 10$ a slight divergence can be observed as the erosion rate is further decreasing when the asymptotic state is approached. Since we are mainly interested in the phases with substantial sediment transport, the duration of the experiments was not chosen long enough to reach this asymptotic state. Other studies such as by Rajaratnam and Berry (1977); Rajaratnam and Mazurek (2002); Sequeiros et al. (2007), chose the transition time to the asymptotic state and the value of $h_{s,\max}$ at the equilibrium state as scaling parameters to achieve the collapse of data for the final stage of erosion. As a consequence, the earlier stages of erosion could not be scaled properly in their case.

According to Di Nardi et al. (2022), during the developed phase (i.e., for $t > t^*$), the "scour hole evolves homothetically, leading to a geometric similarity of the scour profiles", and the aspect ratio of the hole $L_s/h_{s,\max}$ tends to constant values. Therefore, we first have a look at the angle of the upstream and downstream faces of the scour hole, $\theta_{s,up}$ and $\theta_{s,down}$, respectively, as depicted in Figure 6. In this figure, the time evolution of $\theta_{s,up}$ and $\theta_{s,down}$ can be visualized. Although these angles depend on other parameters besides $h^*_{s,\max}$, the time scale for transition is similar, as seen in Figure 6 for $t/t^* > 1$, where a convergence toward an equilibrium value can be observed.

For $t > t^*$, $\theta_{s,down}$ tends to an equilibrium around $\approx 38° \pm 6\%$. It is likely that the flow exiting the hole creates a slope slightly steeper than the angle of repose ($33° \pm 5\%$). The upstream slope $\theta_{s,up}$ ($\approx 33° \pm 10\%$) is similar to the

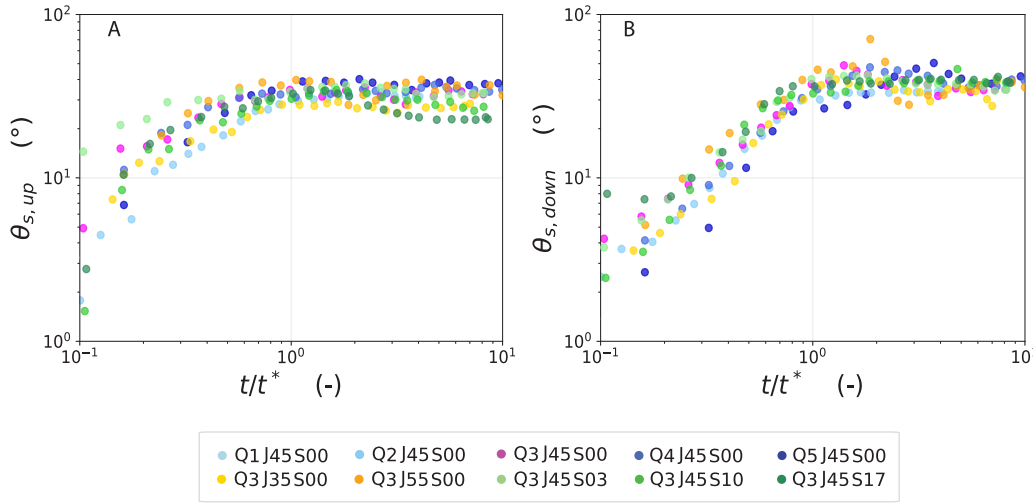

Figure 6. Temporal evolution of (a) angle of the upstream face of the scour hole ($\theta_{s,up}$); (b) angle of the downstream face of the scour hole ($\theta_{s,down}$).

angle of repose. Notably, when the bed slope is increased ($\theta_S > 0$), $\theta_{s,up}$ attains a slightly smaller value in accordance with the reduced angle of repose for the sediment, as with case *Q3J45S17*.

To further expand on the self-similarity of scour hole profiles, the depth and length of the hole were scaled on their maximum values according to $y/h_{s,\max}$ versus $(x - x_{s,down})/Ls$ (Di Nardi et al., 2022), for $x < x_{s,down}$. The result is shown in Figure 7 for $t > t^*$, indicating that the shape of the hole is generally the same during its evolution over time for all experimental settings. For the cases where $\theta_S >$ zero, some additional erosion was found at the upstream face because of the steepening of the mobile bed which reduces the angle of repose for the sediment. To compensate for this, we modified the horizontal length scale of the self-similar scour hole longitudinal profiles according to $(x - x_{s,down})(1 + \sin\theta_S)$. This allows for a more representational comparison with the experiments using a horizontal bed.

As a consequence of the observed self-similar shape of the scour hole, the eroded mass per unit width is proportional to $h_{s,\max}{}^2$. Therefore the self-similar erosion process can be captured with:

$$\frac{m_s(t)}{W} \approx \rho_{d,0}\tilde{C}_s h_{s,\max}{}^2 \left(\frac{t}{t^*}\right)^{0.6} \quad t > t^* \tag{12}$$

in which $\tilde{C}_s \approx 1.8$ (±11%) is a shape factor based on the area and the maximum depth of the scour hole for $1 < t/t^* < 10$.

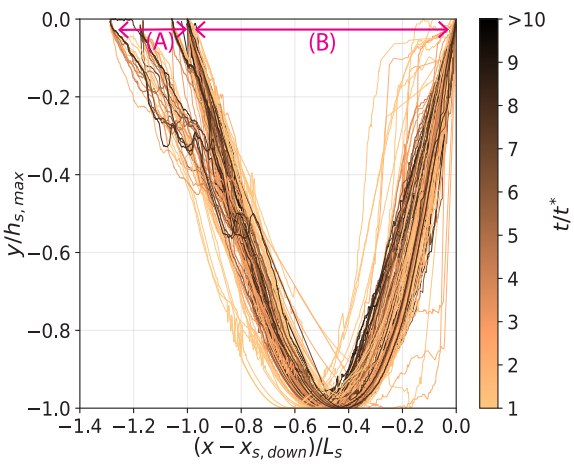

Figure 7. Self-similar longitudinal profiles of the scour hole for all experiments (except *Q1J45S00*) over time ≥ t^*. (a) Indicates the extension of the upstream erosion of the scour hole, $(x - x_{s,down})/L_s < -1$, attributed to the increased bed angle, 17° for the case shown by (A); whereas (B), $-1 \le (x - x_{s,down})/L_s \le 0$ for all the experiments, indicates the length of the scour hole.

3.3. Downstream Deposit Evolution

As suggested by the work of Nomura et al. (2022), Rooij et al. (2009) and Pirmez and Imran (2003), the profiles of the sediment deposits downstream of the scour hole, in the turbidity current region (see Figure 1), follow an exponential decay (Equation 6). The exponential fits for each profile within the base experiment (*Q3J45S00*) are visualized in Figure 8a.

In this study, we employ the two properties from the exponential decay as characteristic scales: h_0 as the height and L_{exp} as the decay length scale, which is equivalent to the center of mass of the deposit generated by the turbidity current. Here, for $x > x_{s,down}$, the origin of the x coordinate is set at $x_{d,max}$, instead of $x_{s,down}$. The outcome is presented in Figure 8b, showcasing dimensionless longitudinal deposit profiles for $t > t^*$ (quasi-steady phase, i.e., the head of the turbidity current is far away, see Figure 4) across all

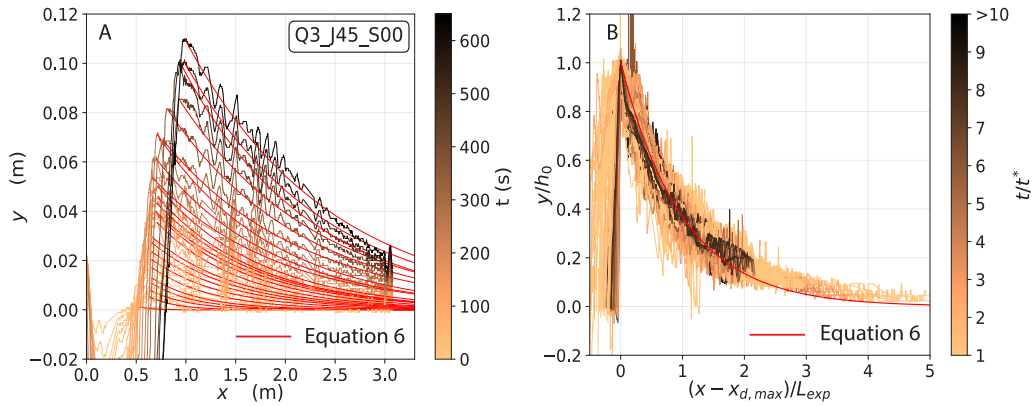

Figure 8. Evolution of the deposit generated by the turbidity current. (a) exponential fits (see Equation 6) for base experiment (*Q3J45S00*); (b) Self-similar longitudinal profiles of the deposit generated by the turbidity current for all experiments (except *Q1J45S00*) and $t > t^*$.

experiments. As all curves collapse within a rather narrow band, it reveals a consistent exponential profile shape for all conditions.

Such profiles allow to determine the amount of deposited sediment given the two parameters h_0 and L_{exp} by simply integrating the exponential function analytically, even if the tail of the deposit is found outside the region of observation. Combining this information and the other contributions we can compare the inferred total mass deposited to the total eroded mass, as described in Equation 1. The ratio of deposited and eroded masses is visualized in Figure 9a for $t/t^* < 10$. Initially, the mass balance is not closed as we neglect the amount of sediment that is in suspension, which can be significant when the relative amount of total eroded material is still small. As time progresses, the accuracy of determination of the mass contributions increases, and the fraction in suspension becomes relatively small, resulting in a ratio approaching unity within a band-width between 80% and 127% for $4 \leq t/t^* \leq 10$. Inaccuracies in the determination of the bed level resulted in outliers particularly for data points of the *Q5J45S00* experiment. The extraction of the bed level profiles for this experiment was particularly difficult, because the high sediment concentration reduced the contrast in the near bed surface.

L_{exp} corresponds to the length of the center of mass and is a measure of the sediment mass deposition distance resultant from the turbidity current transport. Figure 9b shows L_{exp} around different moments in the time series

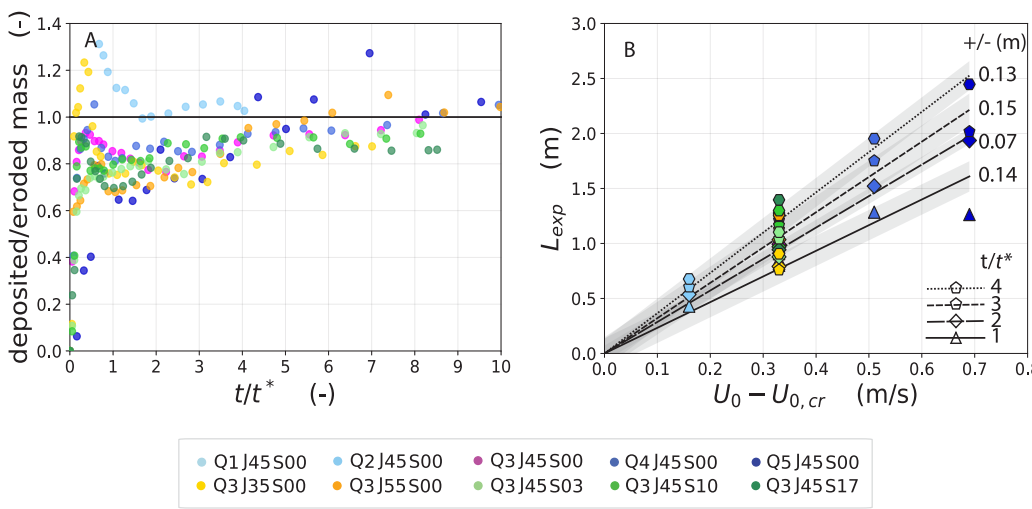

Figure 9. (a) Temporal evolution of ratio between deposited ($m_{d,dun} + m_{d,\exp} + m_{d,up}$) and eroded ($m_s$) masses. (b) Relationship between $L_{\exp}$ with U_0 for $t/t^* = 1$, 2, 3, and 4. The error represented by the gray bar is indicated on the top right corner, at the end of each fit.

(i.e., for $t/t^* = 1, 2, 3$ and 4, an average of the 3 data points nearest in time was taken for L_{exp}) and for the different values of U_0. L_{exp} depends on the jet exit velocity, while the jet and bed angles do not seem to considerably affect it, unlike $h^*_{s,max}$. Note that the slope of the curves do increase with time only weakly. In the next section, we will further analyze the net sediment mass displacement (L_{net}), thereby linking information of the scour hole to the deposit downstream.

3.4. Scaling, Practical Implications, and Limitations

In this section we generalize our findings using the relationships between variables and link the sediment mass displacement length to the jet-induced erosion.

First, a geometrical scale is defined by the thickness of the jet B_0. The approximately constant value of $h^*_{s,max}$ (Figure 5a) suggests the jet thickness to be the dominant length scale here: $h^*_{s,max} \approx 4.9B_0$, as the development of the jet flow itself scales with B_0 as well (see Text S1 in Supporting Information S1, Equations 1 and 3). Second, based on Pagliara et al. (2008), a characteristic time scale $T = B_0/U_c$ is defined, where U_c is a characteristic velocity based on the gravimetric properties of the sediment, that is, $U_c = \sqrt{g'D_{50}}$. Considering the jet and sediment properties in our experiments, $T = 0.84$. The dimensionless jet velocity can then be represented by a Froude number, $\tilde{F}r_{d,0} = U_0/\sqrt{g'D_{50}}$ (similarly to Pagliara et al. (2008); Rajaratnam and Mazurek (2002); Sequeiros et al. (2007)). In this way, dimensionless relationships are derived allowing to generalize our findings. The geometrical scaling gives for $t = t^*$:

$$\tilde{h}^*_{s,max} = \frac{h^*_{s,max}}{B_0} \approx 4.9, \tag{13}$$

whereas the temporal scaling can be expressed in:

$$\tilde{t}^* = \frac{T}{t^*} \approx \tilde{C}_u \left(\tilde{F}r_{d,0}{}^2 \sin\theta_J{}^2 - \tilde{F}r_{d,cr}{}^2\right), \tag{14}$$

where the constant of proportionality is estimated as $\tilde{C}_u \approx 0.13 \cdot 10^{-3}$, complementing Equations 9–12 and allowing to scale the scouring and depositional processes.

The difference between the positions of L_{exp}, discussed in Section 3.3, and the center of mass of the scour hole gives a measure of the net sediment mass displacement distance (L_{net})—see Section 2.7. Based on the findings presented in Figure 9b and the scaling properties just discussed in this section, a simple way of estimating L_{net} is presented in Appendix A.

A quantity that represents the effective result of the jet application is proposed as the product of the net displacement length and the amount of displaced material. This property can be interpreted as proportional to the work done against a force that is proportional to the displaced mass. In Figure 10a, we show the temporal evolution of this final product of the jet application as sediment volume per unit width times net displacement distance, p (m^3), which is calculated as follows:

$$p(t) = \frac{m_{d,down}(t)}{W\rho_{sed}} L_{net}(t), \tag{15}$$

Figure 10a shows the time evolution of p in dimensionless form, where p^* is the value of p at t^*. In summary:

$$\tilde{p}(t) = \frac{p}{p^*} \approx \left(\frac{t}{t^*}\right)^1 \quad \text{for} \quad t > t^*, \tag{16}$$

where p^* (Figure 10b) can be linked to the jet velocity through the densimetric Froude numbers:

$$\tilde{p}^* = \frac{p^*}{B_0{}^3} \approx \tilde{C}_p \left(\tilde{F}r_{d,0} - \tilde{F}r_{d,cr}\right), \tag{17}$$

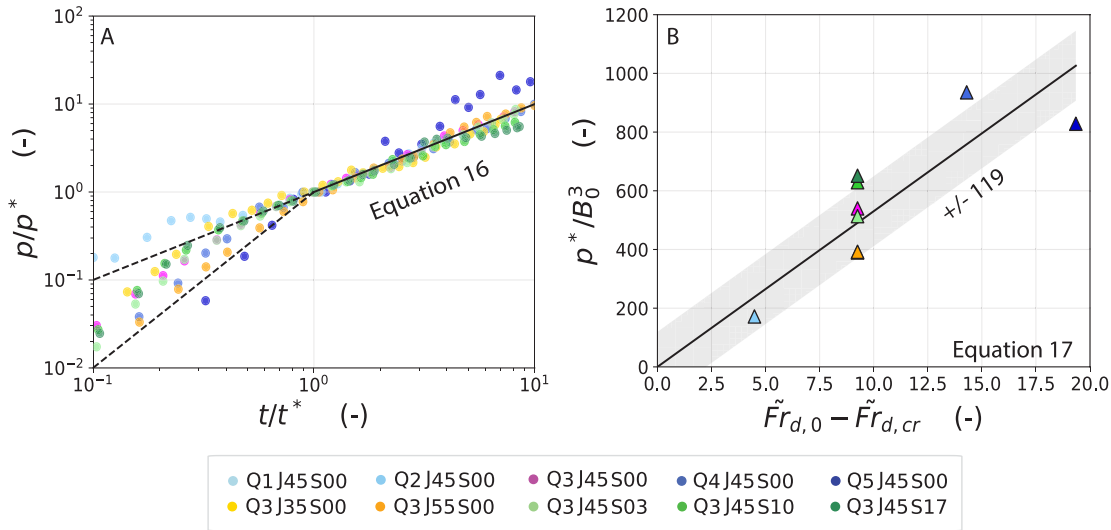

Figure 10. (a) Temporal evolution of the cumulative net sediment volume displacement per unit width (p). (b) Linear relationship between p^* and $\tilde{Fr}_{d,0}$.

with $\tilde{C}_p \approx 53$. In this way a simple and scalable expression is obtained for the net sediment volume displacement per unit width resulting from the jet application. For the second phase ($t > t^*$), p/p^* grows linearly with slope ≈ 1 ($\pm 17\%$). For the first phase ($t < t^*$), the exponent for the time dependency shows larger variations, as it could attain values approximately from 1 up to 2 (see dashed lines in Figure 10a), showing a rate that increases faster than in phase 2. In terms of practical applications, this means that the first erosion mode causes the most efficient jet application outcome.

The evolution of p over time is dominated by the amount of sediment that is eroded. This is suggested by comparing Equation 16, which presents time dependency through the exponent 1, with Equation 12, which presents time dependency through the exponent 0.6. Furthermore, in Appendix A, it is demonstrated that Equation 16 is consistent with the dependencies as found with Equations 12–14, and Figure 9b.

The experiments were designed to optimize the use of the flume to study this technique, and some limitations, which would not exist in a large water reservoir, were imposed by the scale of the experimental installation. An important limitation was the water depth in the flume, which limited the height of the sediment cloud above the scour region during periods of the quasi-steady phase of some experiments (see Figure 4c). In addition, the limited space combined with a large momentum input from the jet could also generate re-circulation zones in the flume. Return currents flowing near the water surface to the upstream direction were observed for the majority of the experiments with speeds of $\mathcal{O}(1)$ cm/s, and circular currents upstream the jet were apparent only in a minority of experiments. These limitations were most evident for experiment *Q5J45S00* (higher discharge). However, we conclude that these effects resultant of the constraining size of the experimental installation on the processes observed in our experiments were limited, as the results for all experiments scaled similarly.

In practice, water injection is usually applied using a wide array of circular jets. Even in environments without lateral confinement as an initial condition, this type of array would generate a quasi two-dimensional-vertical flow (Jirka, 2006; Perng & Capart, 2008), similar to the two-dimensional-vertical configuration we used in this study. However, without lateral confinement, the turbidity current would, unlike in these experiments, generate a fan-shaped deposit. Besides this, the long array of circular jets is usually attached to a moving boat, and, as highlighted by the study of Perng and Capart (2008), the traveling velocity is an important variable defining the scour shape and flow conditions. These differences could be further investigated to expand this study.

The relationships and scaling presented in this study are valid for the tested range of $\tilde{Fr}_{d,0}$ numbers (see Table 1) and $t/t_* < 10$. Besides this, similar grain sizes (i.e., very fine—fine sand) and similar jet thickness (i.e., at least same order of magnitude) should also be taken into account. Furthermore, in our study, the initial impingement distance is equivalent to the length of the potential core ($6B_0$), which limits the spreading of the jet before impinging the initial bed level. If the initial impingement distance would be $>6B_0$, a corrected value of U_0 for

$\tilde{Fr}_{d,0}$ and B_0 for $\tilde{h}^*_{s,\max}$ should be considered. This could be implemented by using the self-similar jet properties described in the Text S1 of Supporting Information S1.

Within the parameter range of this study the role of the jet momentum is apparent, so the erosion process can be linked to the Shields parameter, thereby accounting for the jet properties at impact (such as the induced shear velocity, u_*), which is governed by the exit jet velocity (U_0). This is also suggested by the introduction of densimetric Froude numbers in Section 3.4. Based on the observed critical densimetric Froude number for occurrence of relevant erosion and deposition processes ($Fr_{d,0} = 4.6$, for experiment $Q1J45S00$, as confirmed by Figure 5d), and the critical Shields number for incipient motion of particles used in this study (≈ 0.06), we arrive at a ratio $u_*/U_0 \approx 0.05$.

Considering $u_*/U_0 \approx 0.05$, the Shields $\left(\frac{u_*}{g' D_{50}}\right)$, particle Reynolds $\left(\frac{u_* D_{50}}{\nu}\right)$, and Rouse $\left(\frac{\omega}{u_*}\right)$ numbers of our experiments range between ≈0.05–1.4, 1.8–9.4, and 12–4, respectively, at the initial impingement region. Assuming application by the same jet, the light-weight particles used in this study fulfill the Shields and Rouse similarity requirements (thus adequately reproducing the sediment transport processes at the scour region) for natural sand with a material density of 2,650 kg/m^3, grain sizes 29% smaller, and jet velocities 42% higher (Hughes, 1995; Julien, 2002). In addition, considering the time scale T, these processes would evolve 29% faster.

More research needs to be conducted particularly with different grain sizes, jet design (B_0), initial impingement distance, and larger exit jet momentum inputs to corroborate the proposed scaling and further extend the range of application.

4. Conclusions

Based on 10 controlled laboratory experiments, we examined how variations in initial and boundary conditions affect the interconnected scour hole erosion and downstream deposition processes triggered by a water jet impinging on a mobile bed.

A relevant result was the identification of two distinct transport modes for the scour flow, related to an important time scale in the scour hole development (Pagliara et al., 2008). In addition, the self-similar nature of the longitudinal profiles of both the scour hole and downstream deposit during the indirect transport mode, reinforced the idea that the processes follow predictable scaling laws.

Besides this, the jet's exit velocity, expressed in dimensionless form as the jet densimetric Froude number, emerged as the key controlling variable in our experiments. Finally, we introduced a quantitative metric — the cumulative net displacement volume per unit width, which can serve as a tool for optimizing and comparing different experimental setups and real-world applications.

With this study, we improved our fundamental understanding of this sediment management technique, and the findings presented here can help to improve predictive models. Future research could expand the scope of our experiments and analysis to investigate how these findings can be further generalized. This particularly holds for the role of the turbidity current as the main distal transporting agent.

Appendix A: Equations to Predict Net Sediment Volume Displacement per Unit Width (p)

Below it will be clarified that we can arrive at virtually the same result as Equations 16 and 17 by rearranging Equation 15 for the earlier (Equations 12 and 13) and newly (Equations A1–A4) identified relationships.

The displaced mass, $m_{d,down}(t)/W$ can be written as a fraction of $m_s(t)/W$:

$$\frac{m_{d,down}(t)}{W} \approx \tilde{C}_m \frac{m_s(t)}{W}, \tag{A1}$$

and the net displacement distance L_{net} can be estimated via the relationship:

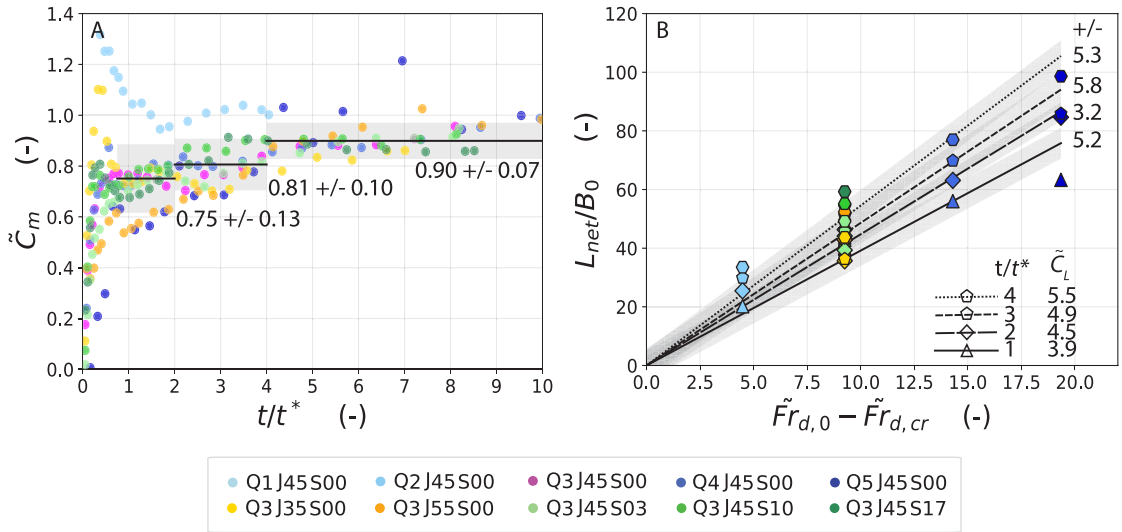

Figure A1. (a) Temporal evolution of the mass conservation parameter $\tilde{C}_m$. (b) Temporal evolution of the mas displacement parameter $\tilde{C}_L$. The error represented by the gray bar is indicated on the top right corner, at the end of each fit.

$$\tilde{L}_{net} = \frac{L_{net}}{B_0} \approx \tilde{C}_L \left(\tilde{F}r_{d,0} - \tilde{F}r_{d,cr}\right), \tag{A2}$$

where both $\tilde{C}_m$ and $\tilde{C}_L$ are only varying slightly with time within the range $0.75 < t/t^* < 10$ and $1 < t/t^* < 4$, respectively, as shown in Figure A1. These variations can be approximately translated to:

$$\tilde{C}_m \approx 0.75\left(\frac{t}{t^*}\right)^{0.11} \quad \text{for} \quad t > t^*, \tag{A3}$$

$$\tilde{C}_L \approx 3.9\left(\frac{t}{t^*}\right)^{0.24} \quad \text{for} \quad t > t^*. \tag{A4}$$

Finally, reformulating Equation 15 with use of Equations 12 and 13, and A1–A4 results in:

$$p(t) \approx \tilde{C}_m\left(\frac{t}{t^*}\right)^{0.11} \frac{\rho_{d,0}}{\rho_{sed}} \tilde{C}_s \left(\tilde{h}^*_{s,\max} B_0\right)^2 \left(\frac{t}{t^*}\right)^{0.60} B_0 \tilde{C}_L \left(\frac{t}{t^*}\right)^{0.24} \left(\tilde{F}r_{d,0} - \tilde{F}r_{d,cr}\right) \quad \text{for} \quad t > t^*, \tag{A5}$$

which can be simplified to:

$$\tilde{p}(t) = \frac{p(t)}{B_0^{\,3}} \approx \tilde{C}_t \left(\tilde{F}r_{d,0} - \tilde{F}r_{d,cr}\right) \left(\frac{t}{t^*}\right)^{0.95} \quad \text{for} \quad t > t^*, \tag{A6}$$

in which $\tilde{C}_t$ absorbs all dimensionless constants ($\tilde{C}_m, \tilde{h}^{*2}_{s,\max}, \tilde{C}_s, \tilde{C}_L, \frac{\rho_{d,0}}{\rho_{sed}} = 0.465$) from the fitting procedures so far, resulting in $\tilde{C}_t \approx 59$, which, for $t = t^*$, can be considered equivalent to $\tilde{C}_p$ from Equation 17 (≈ 53). Besides this, the time dependency exponent of both Equations 16 and A6 are similar (≈ 1). Furthermore, in relation to results obtained via Equations 16 and 17, Equation A6 overestimates p by $\approx 7\%$, an amount that is considered within experimental error.

The above inferred scaling of the processes has limited precision. Nevertheless, it provides insight in the contributions to the erosion and deposition processes, as well as guidance to the interpretation of our findings.

Data Availability Statement

The data set underlying this study is available at 4TU.ResearchData via https://doi.org/10.4121/47f474f1-cdf5-470f-9121-0a290f327cae.v1 (Buffon et al., 2025) with a CC BY 4.0 license (https://creativecommons.org/licenses/by/4.0/).

Acknowledgments
We thank CAPES Foundation for P. Buffon's personal Grant Ph.D. Abroad 88881.174820/2018–01, and DAAD for P. Buffon's personal Grant Bi-nationally Supervised Doctoral Degree 2022/23 (57588368). We thank the Section Rivers of TU Delft and Lammingafonds for supplemental funding, and the TU Delft Open Access Fund. We thank IHE Delft - Institute for Water Education, Department of Water Resources and Ecosystems, Delft, the Netherlands, where early stages of this research were carried out. We thank the Hydraulic Engineering laboratory of TU Delft, where the experiments were carried out, in particular A. van der Vlies, A. Doorn, C. Willems, F. Kalkman, P. van der Gaag, S. de Vree, A. Middeldorp (Waterlab), and W. Bakker (Deltares) for their technical support. We also thank J. Eggenhuisen from Utrecht University for kindly lending an UVP probe. Finally, we thank two anonymous reviewers and P. Nelson (associate editor) for their constructive reviews.

References

Annandale, G. W., Morris, G. L., & Karki, P. (2016). *Extending the life of reservoirs: Sustainable sediment management for dams and run-of-river hydropower*. The World Bank. https://doi.org/10.1596/978-1-4648-0838-8

Baena-Escudero, R., Guerrero-Amador, I. C., Rinaldi, M., & González-Sayago, A. (2021). Hydrological and geomorphic effects upstream of the cantillana dam along the guadalquivir river (Southern Spain). *Geomorphology*, *388*, 107786. https://doi.org/10.1016/j.geomorph.2021.107786

Birman, V., Meiburg, E., & Kneller, B. (2009). The shape of submarine levees: Exponential or power law? *Journal of Fluid Mechanics*, *619*, 367–376. https://doi.org/10.1017/S0022112008004862

Bombardelli, F. A., Palermo, M., & Pagliara, S. (2018). Temporal evolution of jet induced scour depth in cohesionless granular beds and the phenomenological theory of turbulence. *Physics of Fluids*, *30*(8), 085109. https://doi.org/10.1063/1.5041800

Boulange, J., Hanasaki, N., Yamazaki, D., & Pokhrel, Y. (2021). Role of dams in reducing global flood exposure under climate change. *Nature Communications*, *12*(1), 417. https://doi.org/10.1038/s41467-020-20704-0

Buffon, P., Uijttewaal, W. S. J., Valero, D., & Franca, M. J. (2025). Dataset underlying the study "Evolution of erosion and deposition induced by an impinging jet to manage sediment". Version 1. [Dataset]. *4TU.ResearchData*. https://doi.org/10.4121/47F474F1-CDF5-470F-9121-0A290F327CAE.V1

Burke, E. R., Tront, J. M., Lyon, K. N., Rex, W., Castera Errea, M. I., Varughese, M. C., et al. (2023). *What the future has in store: A new paradigm for water storage—overview for policy makers*. World Bank Group. Retrieved from http://documents.worldbank.org

Caretta, M., Mukherji, A., Arfanuzzaman, M., Betts, R., Gelfan, A., Hirabayashi, Y., et al. (2022). Chapter 4: Water. In *Climate change 2022: Impacts, adaptation and vulnerability. Contribution of working group II to the sixth assessment report of the intergovernmental panel on climate change* (pp. 551–712). Cambridge University Press. https://doi.org/10.1017/9781009325844.006

Chamoun, S., Cesare, G. D., & Schleiss, A. J. (2018). Venting of turbidity currents approaching a rectangular opening on a Horizontal bed. *Journal of Hydraulic Research*, *56*(1), 44–58. https://doi.org/10.1080/00221686.2017.1289266

Di Nardi, J., Palermo, M., Bombardelli, F. A., & Pagliara, S. (2022). First principles-based approach for 3d scour processes under variable jet discharge. *Water Resources Research*, *58*(11). https://doi.org/10.1029/2021WR030346

Ezcurra, E., Barrios, E., Ezcurra, P., Ezcurra, A., Vanderplank, S., Vidal, O., et al. (2019). A natural experiment reveals the impact of hydroelectric dams on the Estuaries of tropical rivers. *Science Advances*, *5*(3), eaau9875. https://doi.org/10.1126/sciadv.aau9875

Fan, J., & Morris, G. L. (1992). Reservoir sedimentation. I: Delta and density current deposits. *Journal of Hydraulic Engineering*, *118*(3), 354–369. https://doi.org/10.1061/(ASCE)0733-9429(1992)118:3(354)

Hughes, S. A. (1995). In P. L. F. Liu (Ed.), *Physical models and laboratory techniques in coastal engineering*. World Scientific.

ICOLD. (2024). International comission on large dams: World register of dams. Retrieved from https://www.icold-cigb.org/

Jirka, G. H. (2006). Integral model for turbulent buoyant jets in unbounded stratified flows part 2: Plane jet dynamics resulting from multiport diffuser jets. *Environmental Fluid Mechanics*, *6*(1), 43–100. https://doi.org/10.1007/s10652-005-4656-0

Julien, P. Y. (2002). *River mechanics*. Cambridge University Press.

Kirichek, A., Cronin, K., de Wit, L., & van Kessel, T. (2021). Advances in maintenance of ports and waterways: Water injection dredging. In A. J. Manning (Ed.), *Sediment transport (chap. 6)*. IntechOpen. https://doi.org/10.5772/intechopen.98750

Kondolf, G. M., Gao, Y., Annandale, G. W., Morris, G. L., Jiang, E., Zhang, J., et al. (2014). Sustainable sediment management in reservoirs and regulated rivers: Experiences from five continents. *Earth's Future*, *2*(5), 256–280. https://doi.org/10.1002/2013EF000184

Kondolf, G. M., Schmitt, R. J. P., Carling, P. A., Goichot, M., Keskinen, M., Arias, M. E., et al. (2022). Save the mekong delta from drowning. *Science*, *376*(6593), 583–585. https://doi.org/10.1126/science.abm5176

Latrubesse, E. M., Arima, E. Y., Dunne, T., Park, E., Baker, V. R., d'Horta, F. M., et al. (2017). Damming the rivers of the Amazon basin. *Nature*, *546*(7658), 363–369. https://doi.org/10.1038/nature22333

Ma, H., Nittrouer, J. A., Fu, X., Parker, G., Zhang, Y., Wang, Y., et al. (2022). Amplification of downstream flood stage due to damming of fine-grained rivers. *Nature Communications*, *13*(1), 3054. https://doi.org/10.1038/s41467-022-30730-9

Mao, J., Si, J.-H., Chen, J., Li, G., & Wang, X. (2023). Experimental investigation on sand bed scour by an oblique planar water jet at varying impinging angles. *Ocean Engineering*, *279*, 114526. https://doi.org/10.1016/j.oceaneng.2023.114526

Nomura, S., De Cesare, G., Furuichi, M., Takeda, Y., & Sakaguchi, H. (2022). Spatio-temporal deposition profile of an experimentally produced turbidity current with a continuous suspension supply. *International Journal of Sediment Research*, *37*(3), 299–306. https://doi.org/10.1016/j.ijsrc.2021.11.004

Pagliara, S., Hager, W. H., & Unger, J. (2008a). Temporal evolution of plunge pool scour. *Journal of Hydraulic Engineering*, *134*(11), 1630–1638. https://doi.org/10.1061/(ASCE)0733-9429(2008)134:11(1630)

Perng, A., & Capart, H. (2008). Underwater sand bed erosion and internal jump formation by travelling plane jets. *Journal of Fluid Mechanics*, *595*, 1–43. https://doi.org/10.1017/S0022112007008567

PIANC. (2013). Injection dredging, pianc report no. 120. PIANC, the world association for Waterborne transport infrastructure. Retrieved from https://app.knovel.com/hotlink/toc/id:kpIDPIANC4/injection-dredging-pianc/injection-dredging-pianc

Pirmez, C., & Imran, J. (2003). Reconstruction of turbidity currents in amazon channel. *Marine and Petroleum Geology*, *20*(6), 823–849. (Turbidites: Models and Problems). https://doi.org/10.1016/j.marpetgeo.2003.03.005

Rajaratnam, N. (1976). *Turbulent jets*. Elsevier.

Rajaratnam, N., & Berry, B. (1977). Erosion by circular turbulent wall jets. *Journal of Hydraulic Research*, *15*(3), 277–289. https://doi.org/10.1080/00221687709499648

Rajaratnam, N., & Mazurek, K. (2002). Erosion of a polystyrene bed by obliquely impinging circular turbulent air jets. *Journal of Hydraulic Research*, *40*(6), 709–716. https://doi.org/10.1080/00221680209499917

Randle, T. J., Morris, G. L., Tullos, D. D., Weirich, F. H., Kondolf, G. M., Moriasi, D. N., et al. (2021). Sustaining United States reservoir storage capacity: Need for a new paradigm. *Journal of Hydrology*, *602*, 126686. https://doi.org/10.1016/j.jhydrol.2021.126686

Rooij, D. F., Dalziel, S., & Mccaffrey, W. (2009). Particulate gravity currents. In *Time- and space-resolved measurements of deposition under turbidity currents* (pp. 207–215). Blackwell Publishing Ltd. https://doi.org/10.1002/9781444304275.ch15

Schleiss, A. J., Franca, M. J., Juez, C., & Cesare, G. D. (2016). Reservoir sedimentation. *Journal of Hydraulic Research*, *54*(6), 595–614. https://doi.org/10.1080/00221686.2016.1225320

Schmitt, R. J. P., Bizzi, S., Castelletti, A., & Kondolf, G. M. (2018). Improved trade-offs of hydropower and sand connectivity by strategic dam planning in the mekong. *Nature Sustainability*, *1*(2), 96–104. https://doi.org/10.1038/s41893-018-0022-3

Sequeiros, O. E., Cantero, M. I., & Garcia, M. H. (2009). Sediment management by jets and turbidity currents with application to a reservoir for flood and pollution control in Chicago, Illinois. *Journal of Hydraulic Research*, *47*(3), 340–348. https://doi.org/10.1080/00221686.2009.9522005

Sequeiros, O. E., Niño, Y., & Garcia, M. H. (2007). Erosion of finite thickness sediment beds by single and multiple circular jets. *Journal of Hydraulic Engineering*, *133*(5), 495–507. https://doi.org/10.1061/(ASCE)0733-9429(2007)133:5(495)

Shelley, J., Hotchkiss, R. H., Boyd, P., & Gibson, S. (2022). Discharging sediment downstream: Case studies in cost effective, environmentally acceptable reservoir sediment management in the United States. *Journal of Water Resources Planning and Management*, *148*(2), 05021028. https://doi.org/10.1061/(ASCE)WR.1943-5452.0001494

Syvitski, J. P. M., Vörösmarty, C. J., Kettner, A. J., & Green, P. (2005). Impact of Humans on the flux of terrestrial sediment to the global coastal ocean. *Science*, *308*(5720), 376–380. https://doi.org/10.1126/science.1109454

Wang, Z.-Y., & Hu, C. (2009). Strategies for managing reservoir sedimentation. *International Journal of Sediment Research*, *24*(4), 369–384. https://doi.org/10.1016/S1001-6279(10)60011-X

Warrick, J. A., Stevens, A. W., Miller, I. M., Harrison, S. R., Ritchie, A. C., & Gelfenbaum, G. (2019). World's largest dam removal reverses coastal erosion. *Scientific Reports*, *9*(1), 13968. https://doi.org/10.1038/s41598-019-50387-7

Winterwerp, J. C., Wang, Z. B., van Kester, J. A. T. M., & Verweij, J. F. (2002). Far-field impact of water injection dredging in the crouch river. In *Proceedings of the institution of civil engineers—water and maritime engineering 2002* (Vol. 154, pp. 285–296). https://doi.org/10.1680/wame.2002.154.4.285

Wisser, D., Frolking, S., Hagen, S., & Bierkens, M. F. P. (2013). Beyond peak reservoir storage? A global estimate of declining water storage capacity in large reservoirs. *Water Resources Research*, *49*(9), 5732–5739. https://doi.org/10.1002/wrcr.20452

Zarfl, C., Berlekamp, J., He, F., Jähnig, S. C., Darwall, W., & Tockner, K. (2019). Future large hydropower dams impact global freshwater megafauna. *Scientific Reports*, *9*(1), 18531. https://doi.org/10.1038/s41598-019-54980-8

References From the Supporting Information

Baas, J. H., Baker, M. L., Buffon, P., Strachan, L. J., Bostock, H., Hodgson, D., et al. (2022). Blood, lead and spheres: A hindered settling equation for sedimentologists based on metadata analysis. *The Depositional Record*, *8*(2), 603–615. https://doi.org/10.1002/dep2.176

Carrigy, M. A. (1970). Experiments on the angles of repose of Granular materials. *Sedimentology*, *14*(3–4), 147–158. https://doi.org/10.1111/j.1365-3091.1970.tb00189.x

Kotsovinos, N. E. (1976). A note on the spreading rate and virtual origin of a plane turbulent jet. *Journal of Fluid Mechanics*, *77*(2), 305–311. https://doi.org/10.1017/s0022112076002127

Pagliara, S., Amidei, M., & Hager, W. H. (2008b). Hydraulics of 3d plunge pool scour. *Journal of Hydraulic Engineering*, *134*(9), 1275–1284. https://doi.org/10.1061/(ASCE)0733-9429(2008)134:9(1275)

Pope, S. B. (2000). *Turbulent flows*. Cambridge University Press.